Journal of Fluids and Structures (2002) **16**(8), 1009–1027
doi:10.1006/jfls.2002.0461 available online at http://www.idealibrary.com on IDEAL®

NUMERICAL SIMULATION OF STEADY FLOW IN A COMPLIANT TUBE OR CHANNEL WITH TAPERED WALL THICKNESS

E. B. SHIM

Department of Mechanical Engineering, Kumoh National University of Technology
Kyungbuk Kumi 730-701, Republic of Korea

AND

R. D. KAMM

Department of Mechanical Engineering and Division of Biological Engineering
Massachusetts Institute of Technology, MIT Room 3-260, 77 Massachusetts Ave.
Cambridge, MA 02139, USA

(Received 22 September 2000; and in final form 14 February 2002)

Flow through compliant tubes with linear taper in wall thickness is numerically simulated by finite element analysis. Two models are examined: a compliant channel and an axisymmetric tube. For verification of the numerical method, flow through a compliant stenotic vessel is simulated and compared to existing experimental data. Steady two-dimensional flow in a collapsible channel with initial tension is also simulated and the results are compared with numerical solutions from the literature. Computational results for an axisymmetric tube show that as cross-sectional area falls with a reduction in downstream pressure, flow rate increases and reaches a maximum when the speed index (mean velocity divided by wave speed) is near unity at the point of minimum cross-sectional area, indicative of wave-speed flow limitation or "choking" (flow speed equals wave speed) in previous one-dimensional studies. For further reductions in downstream pressure, the flow rate decreases. Cross-sectional narrowing is significant but localized. For the particular wall and fluid properties used in these simulations, the area throat is located near the downstream end when the ratio of downstream-to-upstream wall thickness is ≤ 2; as wall taper is increased to ≥ 3, the constriction moves to the upstream end of the tube. In the planar two-dimensional channel, area reduction and flow limitation are also observed when outlet pressure is decreased. In contrast to the axisymmetric case, however, the elastic wall in the two-dimensional channel forms a smooth concave surface with the area throat located near the mid-point of the elastic wall. Though flow rate reaches a maximum and then falls, the flow does not appear to be choked.

1. INTRODUCTION

IN MANY PRACTICAL SITUATIONS, the fluid dynamic forces acting on a physiologic vessel cause the walls to undergo significant deformation. These deformations frequently influence the rate of flow through the vessel and can also elicit important biological effects. Examples in the first category include collapse of the veins above the level of the heart, flow limitation during a forced expiration, and the "waterfall effect" in the pulmonary microvascular bed (Kamm & Pedley 1989). Other biological effects arise from the

0889-9746/02/081009 + 19 $35.00/0

deformation of the vessel wall, resulting in altered gene expression or secretion of various agents, cytokines or growth factors, for example.

Numerous studies have been conducted on vessel collapse using experimental or numerical methods. Experiments by Conrad (1969), Brower & Scholten (1975), and Bertram (1986), to name a few, have demonstrated the rich variety and complexity associated with such phenomena as flow limitation and self-excited oscillations. Numerical investigations based on either a lumped parameter or one-dimensional flow models have reproduced many of these same phenomena. These simple approaches worked remarkably well in the prediction of flow limitation (Oates 1975; Shapiro 1977) and large amplitude flow-induced oscillations (Bertram & Pedley 1982). Questions still remained, however, concerning the precise physical mechanism of flow instability in certain types of flutter and, because of the simplifying assumptions on which the analyses were based, they were obviously not capable of addressing issues involving two- or three-dimensional effects.

In order to produce a more realistic simulation, Pedley (1992) first examined steady, two-dimensional flow in a collapsible channel at low Reynolds number using lubrication theory. Extending this work, Luo & Pedley (1995, 1996) solved the full Navier–Stokes equations for steady and unsteady flows, again for a two-dimensional collapsible channel. In these studies, the wall was modelled as an elastic membrane having zero thickness. This is a useful simplification for thin-walled vessels, but one that fails to account for bending stiffness and in-wall shear stresses that are important in a wall of finite thickness, and that provides no information on the stress distribution inside the vessel wall. Heil & Pedley (1995) presented results showing the behavior of an axisymmetric collapsible tube with the thin wall assumption. More recently, Heil (1997) produced a three-dimensional solution of flow through a collapsible tube using a Stokes flow approximation for the fluid and a shell model for the wall. His results accurately reproduce the three-dimensional character of vessel collapse and compare favorably with experiments, but have thus far been restricted to low Reynolds number flow and thin-walled vessels.

Using a finite element code that solves the fully nonlinear equations for the solid and fluid, Bathe & Kamm (1999) recently analyzed flow at high Reynolds number through an axisymmetric stenotic vessel. Though the axisymmetric assumption precluded buckling of the wall, the solutions allowed for significant inertial effects in the fluid and provided detailed information on the stress field within the elastic wall. The deformations computed in that work, however, were relatively small due to the stiffness of the arterial wall and stenosis relative to the magnitude of pressure fluctuations.

In this study, we use the same approach as Bathe & Kamm (1999), but consider two problems with large amplitude wall deformations. Two-dimensional flows in both axisymmetric and planar geometries are considered under conditions that lead to flow limitation. In an attempt to minimize the influence of the downstream rigid attachment point, models of tubes and channels are used that have a linear taper in wall thickness. Flow is induced by a progressive reduction in downstream pressure. Steady solutions for given pressure differences are obtained solving the full Navier–Stokes equations and the equilibrium equations for the solid elastic wall having finite thickness. We examine varying degrees of wall taper to elucidate its effect on vessel collapse. A commercial finite element package, ADINA, is employed to accurately simulate the essential character of fluid–structure interactions. To validate the accuracy of the code, we solve for flow and deformation in a stenotic compliant tube and two-dimensional collapsible channel, and compare the numerical predictions to the existing experimental and numerical data.

2. COMPUTATIONAL MODEL AND METHODS

Two geometries are simulated to investigate flow through flexible-walled vessels, using the commercial package ADINA (Automatic Dynamics Incremental Nonlinear Analysis, Watertown, MA). Response of the elastic wall is analyzed using the standard Lagrangian formulation for which the governing field equations evaluated at each time step in the analysis are

$$\tau_{ij,i} = \rho_s \ddot{u}_i \tag{1}$$

where τ_{ij} is the ijth component of the Cauchy stress tensor ($i,j = 1,2$), $\ddot{u}_i$ is the material particle acceleration in the coordinate i direction, and ρ_s is the density of solid. The comma denotes partial differentiation. ADINA uses a mixed displacement/pressure-based finite element formulation to solve these equations. In the solutions presented here, nine-node axisymmetric quadrilateral elements with quadratic displacement interpolation and linear element pressure are employed.

The governing equations for viscous incompressible fluid flow are obtained from the principles of mass and momentum conservation. The equations in vector notation are

$$\frac{\partial U}{\partial t} + \nabla\cdot(\boldsymbol{F} - \boldsymbol{G}) = \mathbf{0}, \tag{2}$$

where

$$\mathbf{U} = \begin{Bmatrix} \mathbf{0} \\ \rho_f \mathbf{v} \end{Bmatrix}, F = \begin{Bmatrix} \rho_f \mathbf{v} \\ \rho_f \mathbf{vv} \end{Bmatrix}, G = \begin{Bmatrix} \mathbf{0} \\ \boldsymbol{\tau} \end{Bmatrix} \tag{3}$$

and where $\mathbf{v}$ is the velocity vector; ρ_f is fluid density, and $\boldsymbol{\tau}$ is the stress tensor, the components of which are given by

$$\tau_{ij} = -p\delta_{ij} + 2\mu\ e_{ij}. \tag{4}$$

Here, p is fluid pressure, δ_{ij} the Kronecker delta, μ the coefficient of viscosity, and the components of the strain rate tensor are given by

$$e_{ij} = \frac{v_{i,j} + v_{j,i}}{2}. \tag{5}$$

Application of the usual Galerkin finite element discretization for equation (2) yields the following matrix equations in symbolic form:

$$\mathbf{KX} = \mathbf{R}, \tag{6}$$

where $\mathbf{K}$ is the stiffness matrix, $\mathbf{X}$ is the vector of unknown nodal variables (velocities and pressure) and $\mathbf{R}$ contains the external driving forces. Three-node axisymmetric triangular elements with a linear interpolation function for velocity and pressure and an additional bubble velocity function are used to discretize the fluid domain in equation (2). Since the matrix equation above, derived from fluid governing equation (2), is highly nonlinear, it must be solved by an incremental iterative scheme such as the Newton–Raphson method or the method of successive substitution within each time step (Bathe 1996). A similar matrix equation for the solid is derived from application of the variational principle to equation (1) and discretization of the solid solution domain with nine-node axisymmetric quadrilateral elements having a quadratic displacement interpolation function. In the solid matrix equation, the unknown variables are the nodal displacement vectors.

To simulate interactions between the fluid and solid domains, ADINA utilizes the arbitrary Lagrangian–Eulerian (ALE) formulation (Bathe *et al.* 1995) requiring that the momentum equation (2) be modified to account for mesh movement. This necessitates a simple change in the convective term leading to the form given below (Bathe *et al.* 1995):

$$\rho\left[\frac{\delta v_i}{\delta t} + \left(v_j - \frac{\delta d_j}{\delta t}\right) v_{i,j}\right] = \tau_{ij,j}, \tag{7}$$

where $\delta v_i/\delta t$ is the time derivative of the velocity component v_i at the position of the moving mesh point considered, and $\delta d_j/\delta t$ is the velocity of the moving mesh in the jth direction.

Solution of the fluid and solid equations is accomplished by a fully coupled method satisfying force equilibrium and matching of the velocities and displacements at each nodal point for each time step during the computation. This is accomplished by an iterative technique between the fluid and solid solvers until attaining the desired convergence.

The above equations are expressed in a form appropriate for unsteady flow. Steady solutions can be obtained by solving these unsteady equations with steady boundary conditions until a time-independent solution is achieved, or by directly solving the steady form, obtained by omitting all time-derivative terms in the above. The solutions presented here are obtained by the second method, since it is more economical of computational time. The equivalence of the methods was checked with several specific cases.

3. RESULTS AND DISCUSSION

3.1. Verification of the Code

ADINA was developed originally for the solution of structural problems, and extended in recent years to add the capability for solving fluid flow or fluid–structure interaction (FSI) problems. Since then, it has been used for a variety of fluid–structure interaction problems in engineering, many of which can be found in the literature (Bathe *et al.* 1995; Bathe & Kamm 1999; Zmindak & Grajciar 1997). In a previous paper by our group, the problem of unsteady flow through a stenotic artery was analyzed using ADINA and shown to be in good agreement with steady flow measurements of the pressure drop across a rigid, localized obstruction. Here we present two more validation studies in which the vessel compliance is a dominant factor.

3.1.1. Flow through a compliant tube with a localized constriction

In order to further test the FSI capabilities of the code, we solve for steady flow through a stenotic compliant tube and compare our results with existing experimental data (Stergiopulos *et al.* 1993). For this computation the working fluid is water and the membrane is made of rubber, modelled here using a standard Mooney–Rivlin model (Haggblad & Sundberg 1983) with constants $C_1 = 3 \times 10^5$ Pa, $C_2 = 1{\cdot}5 \times 10^5$ Pa, $D_1 = 0{\cdot}0$ Pa, $D_2 = 0{\cdot}0$ for an effective Young's modulus of $2{\cdot}7 \times 10^6$ Pa. The ratio of bulk modulus to shear modulus is set equal to 1667, giving Poisson's ratio of 0·4997 in this linear elastic analysis. The geometry of the stenotic tube is shown in Figure 1(a), selected to mimic that used in the experiment of Stergiopulos *et al.* As seen in the figure, the stenosis extends for a length of $L_c = 30$ mm and has an unobstructed diameter D_0 of 8 mm.The stenosis diameter at zero transmural pressure D_s is 2·53 mm so that the severity of the stenosis defined as $[1 - D_s^2/D_0^2] \times 100 = 90\%$. We use the following equation for the shape of the stenosis as is in the case of the experiment of Stergiopulos *et al.*

$$D(x) = D_0 - \frac{D_0 - D_s}{2}\left[1 - \cos\left(\frac{2\pi x}{L_s} + \pi\right)\right]. \tag{8}$$

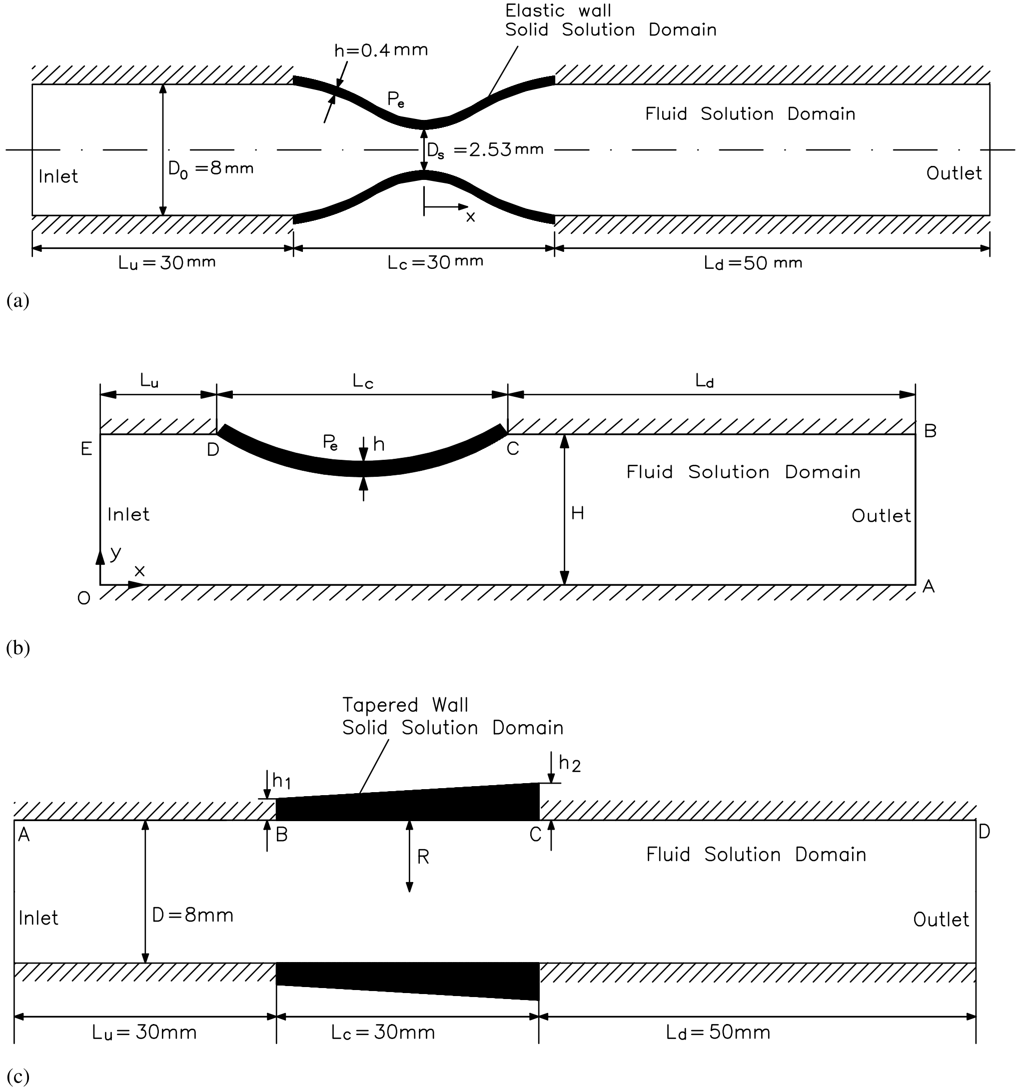

Figure 1. Tube and channel geometries from the present simulations. (a) The stenotic tube with elastic wall as used in the study by Stergiopulos *et al.* (1993); (b) The two-dimensional collapsible channel with initial tension as used by Luo & Pedley (1995); (at points C and D the rigid and flexible walls are fixed at the inner surface.) (c) An axisymmetric compliant tube.

The mesh system of the fluid region is composed of 4848 triangular elements and 2639 nodes and 122 elements and 315 nodes in solid domain.

During the simulation, inlet pressure is held constant at a value of $P_{in} = 74\,\text{mmHg}$ and outlet pressure P_{out} is decreased from 74 mmHg in 1 mmHg increments. External pressure P_e is maintained constant at 3 mmHg. At each pressure, the simulation is continued until the solution becomes steady. This procedure is followed until $P_{out} = 41\,\text{mmHg}$, at which point the numerical solution is no longer able to converge. Since at this stage the Reynolds number based on average outlet velocity and unobstructed diameter is 2478, solutions for lower downstream pressures would be strongly influenced by turbulence, the effects of which are absent from our analysis. In addition, as discussed below, the transmural pressure is beyond that needed to buckle the tube (approximately 27 mmHg based on

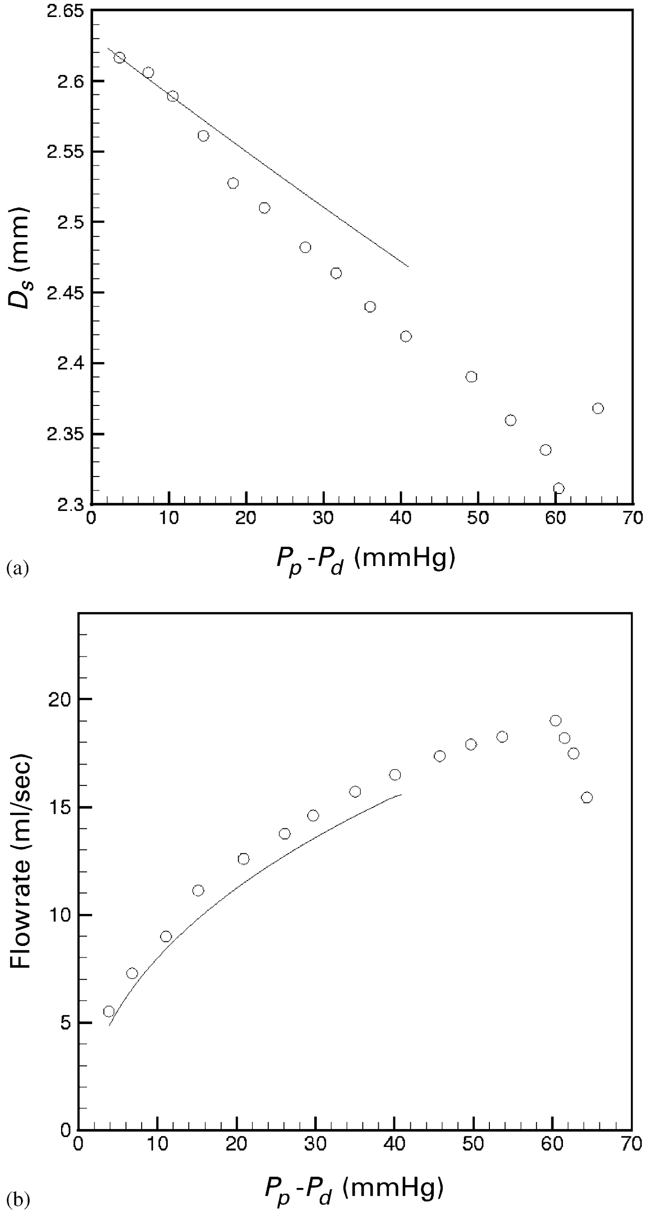

Figure 2. Comparisons of computed results to experimental data by Stergiopulos *et al.* (1993). (a) Stenotic diameter versus pressure difference. (b) Flow rate versus pressure difference. ○, Experimental data; —, Numerical solution.

conditions at the point of minimum diameter), thus invalidating the assumption of axisymmetry.

The streamlines obtained from this solution exhibit a large region of recirculating flow downstream of the stenosis, as one would expect in the vicinity of a sudden expansion. Pressure attains a minimum value at the throat, raising the possibility of collapse of the stenotic tube at that point. Progressing downstream from the stenosis, the pressure increases, corresponding to flow deceleration with some pressure recovery. Figure 2 shows the variations of flow rate and internal diameter of the stenosis as functions of outlet pressure. When the pressure difference is small, there is good agreement between the measured and predicted flow rates and internal diameter of the stenosis. As the pressure difference increases, however, the numerical solutions deviate some from the experimental values, and the computations are terminated at a pressure difference of 41 mmHg prior to the point where the experimental results show flow limitation and tube collapse. For the reasons mentioned above, no attempt was made to continue the calculations beyond this point.

3.1.2. Steady flow through a two-dimensional collapsible asymmetric channel

The results of Luo & Pedley (1995) are chosen for comparison with the steady two-dimensional fluid–structure interaction simulation. Luo & Pedley used the full Navier–Stokes equations to analyze the fluid flow but employed a thin membrane approximation with nonzero initial tension in the compliant wall. The detailed geometry of the problem is depicted in Figure 1(b) and the parameter values used in Luo & Pedley are presented in Table 1. In every instance, we specified the same parameter values used by Luo & Pedley, including the initial wall tension. Additional parameters were required for the solid wall in our simulation, however, due to its finite thickness. To produce a situation that most closely approximates that of a thin membrane in constant tension, we set Young's modulus of the linear elastic solid (E) to a low value (10 Pa) to minimize the change in tension due to membrane deflection. In addition, Poisson's ratio (ν) was set to 0·49 to represent a nearly incompressible material, and the wall thickness was specified to be 2·5% of the channel height H. At points C and D of Figure 1 the flexible wall was fixed to the boundary only at the inner surface, thus allowing the wall slope to be discontinuous where the flexible and rigid walls connect. No-slip boundary conditions were imposed at the wall segments OA, ED, and CB; a parabolic velocity profile was assumed at the entrance EO with zero normal traction at the outflow boundary AB. We calculated the solution for Re = 1 where Reynolds number is based on channel height and the mean velocity at the entrance of the channel for the purpose of comparison to published results.

Luo & Pedley imposed an initial tension in the wall, specified as $T = T_0/\beta$, where T_0 is a constant tension and β is a scaling factor. Higher β implies lower initial tension in the wall and consequently greater deformation for the same transmural pressure difference. Figure 3(a) shows deformed shapes for several values of β and Figure 3(b) indicates the maximum deformation. As can be seen in Figure 3 (a), the agreement with Luo & Pedley [Fig. 4(a) in their paper] is excellent. Deflection of the flexible wall to the right for $\beta = 64$ in Figure 3(a) is similar to that observed by Luo & Pedley. The thin wall is dragged downstream by the viscous stresses that act along the surface of the membrane.

TABLE 1

Parameters used by Luo & Pedley (1995) for simulation of flow through a two-dimensional channel with a thin membrane

Fluid density, ρ	10^3 kg/m^3
Fluid viscosity, μ	10^{-3} kg/(ms)
Reference initial tension, T_0	1·61 N/m
External pressure, P_e	0·93 Pa
Channel height, H	0·01 m
Collapsible length, L_c	0·05 m
Downstream length, L_d	0·07 m
Upstream length, L_u	0·02 m

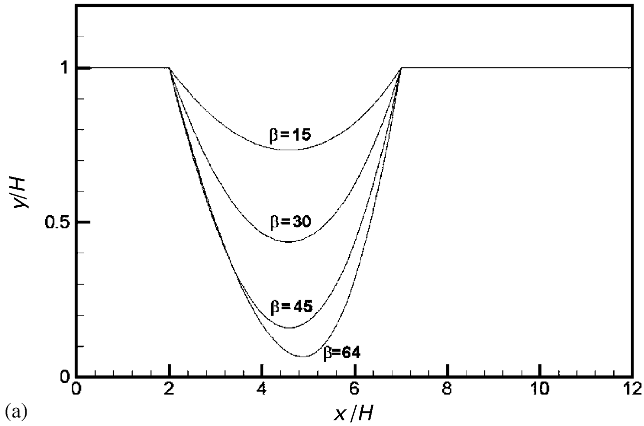

(a)

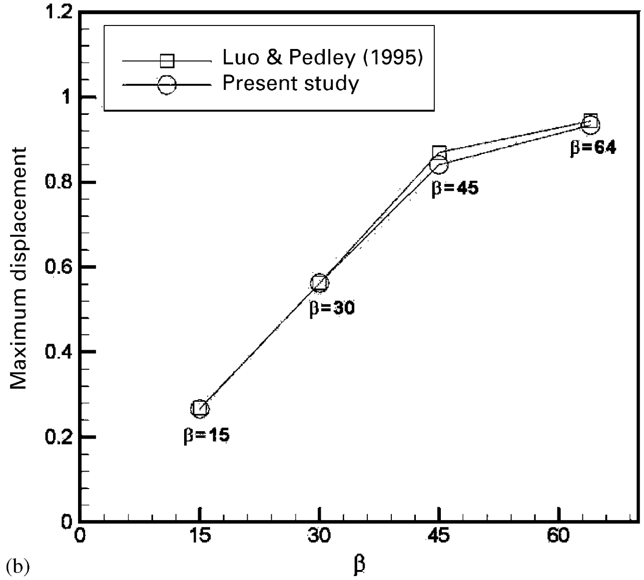

(b)

Figure 3. (a) Deformed shapes of the collapsible wall according to several values of β ($= T_0/T$ where $T_0 = 1{\cdot}61$ N/m). (b) Comparisons of the computed maximum displacement versus β to the results of Luo & Pedley (1995). The minimum channel height is y_{min}.

3.2. AXISYMMETRIC TUBE WITH TAPERED WALL

The axisymmetric model used in the first set of simulations is shown in Figure 1(c). Here, h_1, the upstream wall thickness, is held constant at 0·4 mm. Wall thickness tapers linearly to a maximum value, h$_2$, at the downstream end. The tube length-to-radius ratio, L_c/R, is equal to 7·5 and tapers h_2/h_1 of 1, 2, 3 and 4 are used. The tube wall is taken to be linearly elastic with Young's modulus E of 2×10^3 Pa. All other parameter values are given in Table 2.

A no-slip wall boundary condition is applied in the fluid along lines AB and CD while symmetry is assumed around line EF. Line BC coincides with line IJ of the solid domain constituting the fluid–structure interaction boundary (Figure 4). It is along this boundary that displacements and traction forces are passed between the fluid and solid domains. In these simulations, the fluid and solid domains are discretized as shown in Figure 4. The

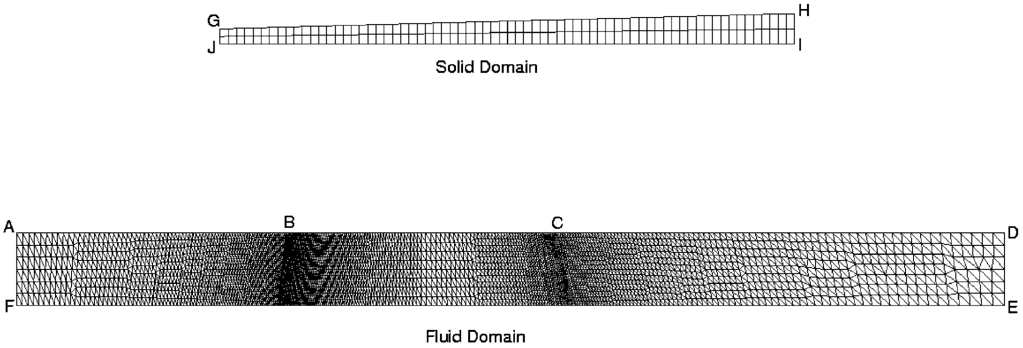

Figure 4. Mesh system for the axisymmetric tube with 6 227 triangular fluid elements and 140 quadrilateral solid elements. (The fluid boundary of line BC is match with the solid boundary line JI.)

Table 2

Material properties and reference values used in simulations of an axisymmetric compliant tube

Fluid density, ρ	$10^3\,\mathrm{kg/m^3}$
Fluid viscosity, μ	$10^{-3}\,\mathrm{kg/(ms)}$
Elastic modulus of solid, E	$2 \times 10^3\,\mathrm{N/m^2}$
Poisson's ratio of solid, v	$0{\cdot}3$
Unobstructed area, $A_0 = \pi R^2$	$5 \times 10^{-4}\,\mathrm{m^2}$
Reference pressure, $P_{\mathrm{ref}} = Eh_1/R$	$200\,\mathrm{Pa}$
Reference flow rate, $Q_{\mathrm{ref}} = \pi R^2(Eh_1/\rho D_0)^{1/2}$	$1{\cdot}58 \times 10^{-4}\,\mathrm{m^3\,s}$

mesh consists of 3 383 nodes, 6 227 triangular elements clustered at both ends of the elastic wall for the fluid domain and 140 quadrilateral elements for the solid domain. To assess mesh dependency, computational results using finer (one-third more mesh points) and coarser (one-third fewer) mesh points for $h_2/h_1 = 1$ produced differences in flow rate and minimum area reduction of less than 2·5%.

Flow is induced by the pressure difference $\Delta P = P_{in} - P_{out}$ between inlet and outlet. Inlet and external pressures are maintained constant at $P_{in} = P_e = 0$ while downstream pressure is decreased in 5 Pa increments, allowing the solution to converge at each condition. The computations are conducted in a stepwise manner using the steady solution from the previous step as the initial guess for the next calculation.

Maximum Reynolds numbers at each wall thickness ratio are given in Table 3 where it is seen that the largest value, 1 200, occurs in the tube with the largest mean wall thickness ($h_2/h_1 = 4$). Streamlines at the condition of maximal pressure difference just prior to loss of convergence are plotted in Figure 5 for the four values of wall thickness ratio. Narrowing is highly localized near the downstream end when the tube is of uniform thickness ($h_2/h_1 = 1$) or when the taper is mild ($h_2/h_1 = 2$). Regions of recirculating flow are observed for these two cases due to the high degree of narrowing and the relatively abrupt area increase downstream of the minimum area point. Figure 6(a,b) shows, flow rate increasing as downstream pressure is reduced, rapidly at first, then slowing, reaching a maximum, and finally falling gradually as the tube becomes increasingly collapsed. This pattern is suggestive of wave speed flow limitation as is often observed in collapsible tube flow (Shapiro 1977), although the drop in flow rate after reaching the peak is not

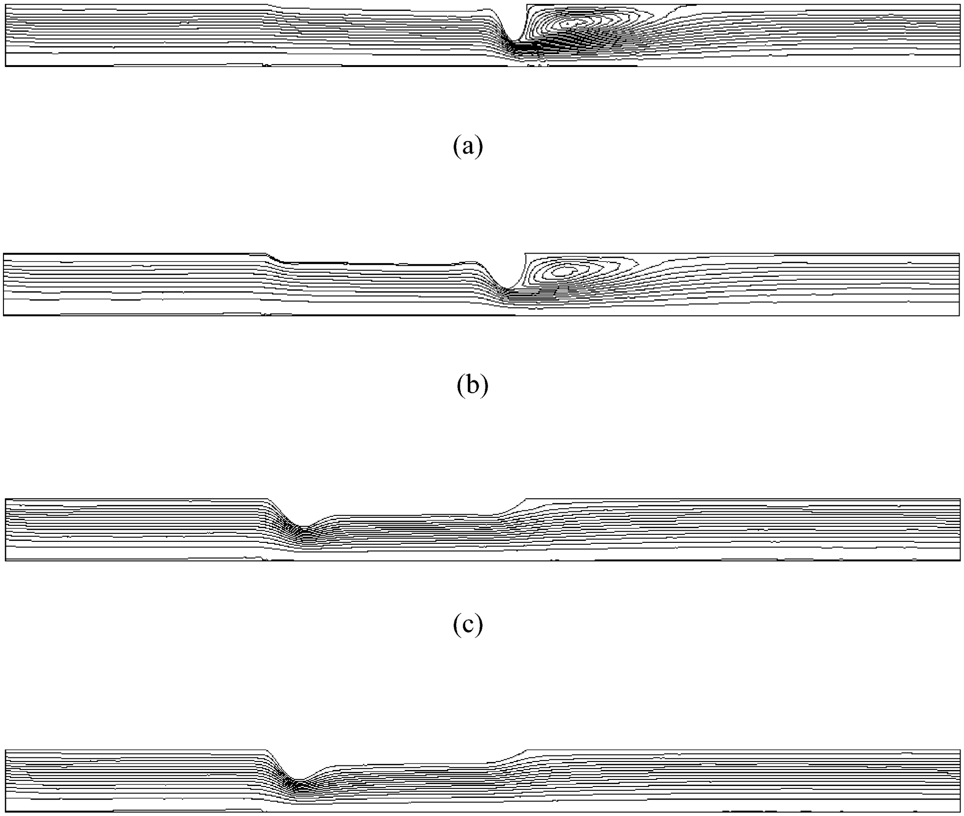

(a)

(b)

(c)

(d)

Figure 5. Streamline patterns in the axisymmetric tube corresponding to the maximum pressure difference before loss of convergence: (a) $h_2/h_1 = 1$ at $\Delta P/P_{ref} = 0{\cdot}9$, (b) $h_2/h_1 = 2$ at $\Delta P/P_{ref} = 1{\cdot}4$, (c) $h_2/h_1 = 3$ at $\Delta P/P_{ref} = 0{\cdot}9$, (d) $h_2/h_1 = 4$ at $\Delta P/P_{ref} = 0{\cdot}9$.

predicted by the previous one-dimensional theories. The speed index (S) of Figure 6 is defined as the ratio of mean fluid speed to wave speed. This behavior is discussed more fully below.

When the degree of wall taper is large [Figure 6(c,d)], the behavior is distinctly different. The point of minimum area moves to a location near the upstream end of the tube, and the recirculation zone is less pronounced or completely absent due to the more gradual area increase downstream. Variations in minimum area are particularly interesting, showing, in contrast to cases with milder taper, an increasingly steep drop as downstream pressure is reduced, up to the point of nonconvergence (Figure 7). In these results, we found no evidence of the axial corrugations in the wall as seen in the axisymmetric results of Heil (1995). This difference is believed to be due to the increased bending stiffness in the present simulations due to a thicker wall than was used in the Heil study. Flow limitation, however, is observed (Figure 6) and follows a pattern that is relatively uninfluenced by the degree of taper. As shown in Table 4, the speed index is approximately equal to unity at the point of maximum flow rate regardless of the degree of taper. These solutions tend to lose convergence soon after maximal flow is attained.

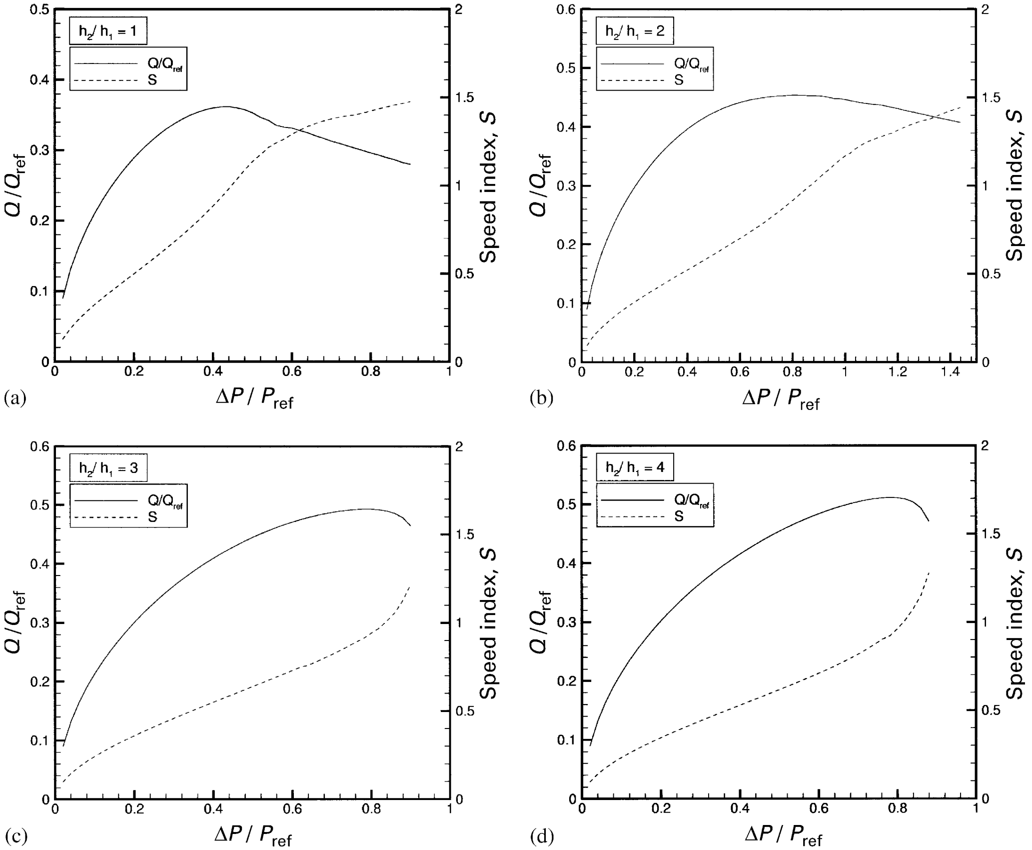

Figure 6. Flow rate and speed index as functions of the inlet-to-outlet pressure difference for (a) $h_2/h_1 = 1$, (b) $h_2/h_1 = 2$, (c) $h_2/h_1 = 3$, (d) $h_2/h_1 = 4$.

The distributions of fluid pressure and solid effective stress are presented for $h_2/h_1 = 2$ in Figure 8. Fluid pressure decreases up to the area minimum, then increases again reflecting a degree of pressure recovery downstream of the throat. Effective stresses in the solid $\sigma_{eff} = \sqrt{\sigma_{yy}^2 + \sigma_{zz}^2}$, where y and z are the directions perpendicular to and parallel to the tube axis, respectively, are large near the downstream end due to the combination of large bending effects and the highly negative transmural pressure.

Here we estimate wave speed for long waves, c, using the Moens–Korteweg equation (Caro 1978)

$$c = (Eh/2\rho_f R)^{1/2}. \tag{9}$$

In this equation, h is the local wall thickness and R is the undeformed radius of tube. In a one-dimensional flow analysis, maximal flow occurs when speed index S = 1 (Shapiro 1977). This is seen to be true in the present simulations (Figure 6 and Table 4) when the speed index, based on mean fluid velocity, evaluated at the point of minimum cross-sectional area is plotted against the pressure difference. Unlike the prediction from purely one-dimensional theory, however, the flow rate is observed to decrease while S continues to rise as downstream pressure is further reduced. Moreover, the profile of S versus axial distance, z/L (Figure 9) continues to change upstream of the point where S = 1, albeit slightly, following the first occurrence of critical flow. These observations could be due to

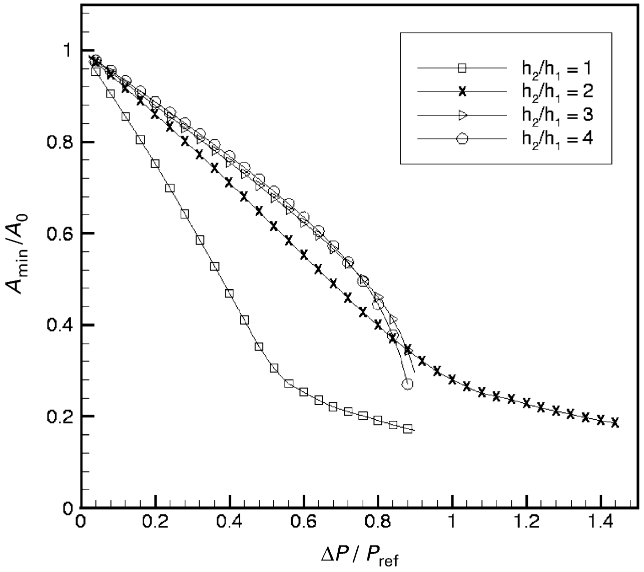

Figure 7. Minimum cross-sectional area in the axisymmetric tube as a function of the inlet-to-outlet pressure difference. Note the difference in character at high collapse for the two cases with large taper as compared to those with small taper.

Table 3

Maximum Reynolds number at each wall thickness ratio in axisymmetric tube simulations

$h_1/h_2 = 1$	$Re_{max} = 910{\cdot}3$
$h_1/h_2 = 2$	$Re_{max} = 1141{\cdot}4$
$h_1/h_2 = 3$	$Re_{max} = 1238{\cdot}8$
$h_1/h_2 = 4$	$Re_{max} = 1285{\cdot}9$

Table 4

Distribution of the value of speed index S at maximum flow rate according to taper degree

	S value
$h_1/h_2 = 1$	0·97
$h_1/h_2 = 2$	0·98
$h_1/h_2 = 3$	0·96
$h_1/h_2 = 4$	0·95

the presence of longitudinal bending stiffness or tension, either of which introduce wave-speed dispersion [so that waves of finite wavelength travel more rapidly than predicted by equation (9)] (McClurken *et al.* 1981). In fact, the possibility of a transition to supercritical flow ($S > 1$) near the downstream attachment point had been observed experimentally and tentatively explained based on an approximate correction to the one-dimensional theory that includes these longitudinal effects (Kececioglu *et al.* 1981).

With larger taper ($h_2/h_1 = 3$ and 4, Figure 6(c,d)), the flow rate once again reaches a maximum when S is approximately one. The fall in flow rate and the increase in speed

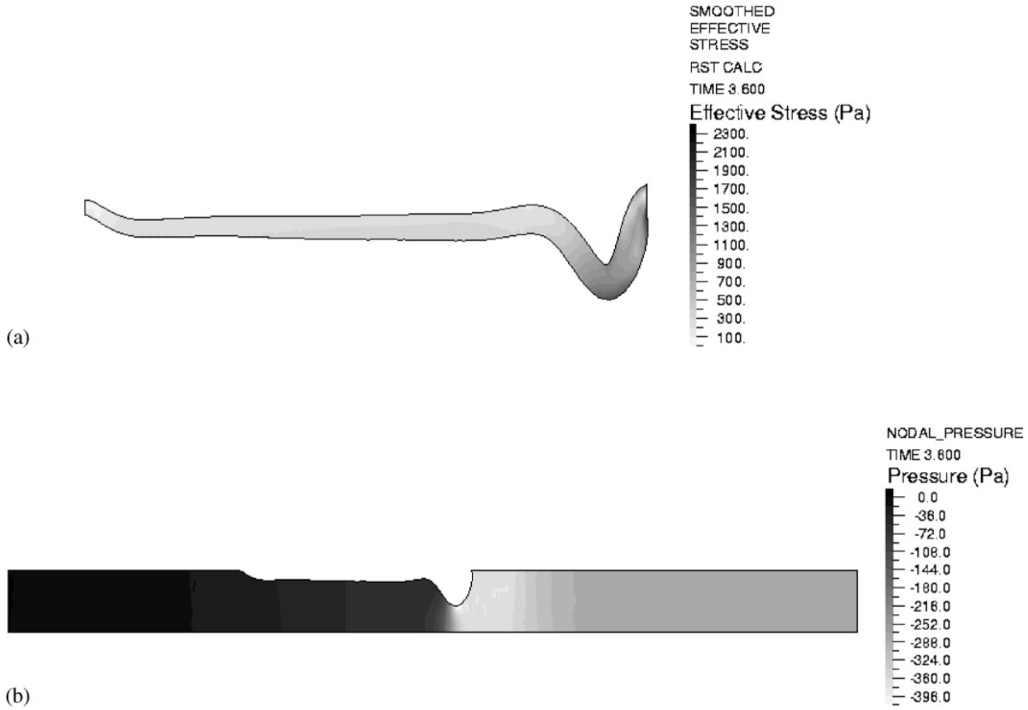

Figure 8. Computed results for the axisymmetric tube with $h_2/h_1 = 2$ just prior to complete collapse. (a) Distribution of effective stress in the elastic wall. (b) Distribution of pressure in the fluid domain.

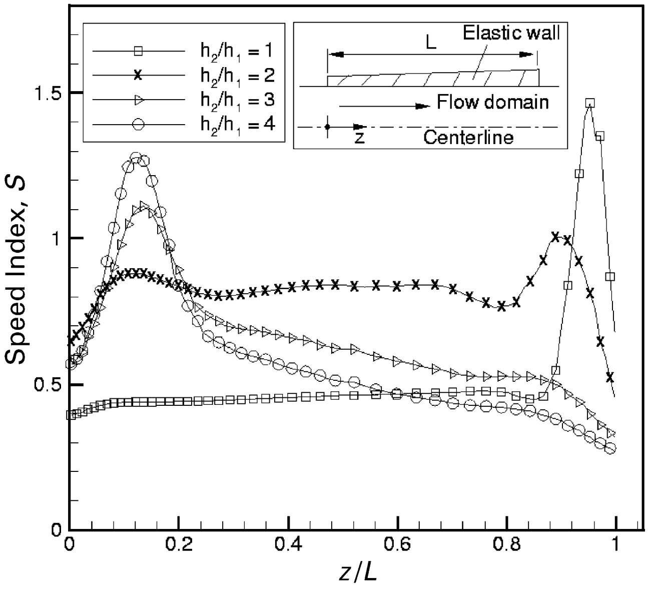

Figure 9. Distribution of speed index as a function of axial distance along the axisymmetric tube at $\Delta P/P_{ref} = 0{\cdot}6$ for each of the four tapered wall configurations.

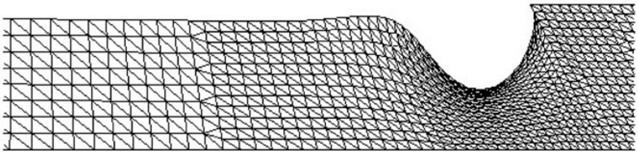

Figure 10. Close-up of the distorted mesh in the axisymmetric tube for $h_2/h_1 = 1$ at $\Delta P/P_{ref} = 0{\cdot}9$ just prior to breakdown of the computation.

index after the point of maximal flow, however, are both more abrupt, and the solution fails to converge much sooner. Note that, in these cases, the point of minimum area and the first occurrence of critical flow are both located near the upstream end of the tube. Downstream of this point the flow accelerates beyond $S=1$, then quickly decelerates to subcritical speeds, continuing to fall in the direction of increasing stiffness. While the transition to subcritical speed appears to be smooth as suggested in previous experiments and one-dimensional theory for tubes with tapered walls (Jaekle 1987), the axisymmetric assumption of the present analysis makes it difficult to make a direct comparison.

In every case, the computations ultimately fail to converge. This occurs at various levels of pressure, but always prior to attaining an outlet pressure of −300 Pa. This may be due to the highly distorted mesh for $h_2/h_1 = 1$ and 2 as shown in Figure 10. In the case of $h_2/h_1 = 3$ and 4, the numerical instability appears to result from the increasingly steep reduction in minimum cross-section area as the outlet pressure decreases (Figure 7). While the cause for lack of convergence in these cases is unknown, it may be indicative of numerical instability, or possibly a breakdown of the steady solution leading to oscillatory behavior. While it may be tempting to speculate as to the relationship between the lack of convergence and the onset of flow-induced oscillations, this is likely premature and will require further, more careful investigation.

Since many of the relevant experiments were conducted on much longer tubes, we examined the effect of tube length by calculating two additional cases for the taper of $h_2/h_1 = 1$: $L/R = 10$ and $L/R = 5$. The flow rates and area reductions of these cases differed by no more than 4% from those of $L/R = 7{\cdot}5$, confirming that the flow phenomena in these simulations are not significantly influenced by tube length.

3.3. Two-dimensional Symmetric Channel with Tapered Wall

The verification problem of two-dimensional collapsible channel presented earlier has been studied extensively by analytical and numerical methods (Rast 1994; Luo & Pedley 1995, 1996*a,b*). While experiments could also be performed in this geometry, none have yet been published, presumably due to the difficulty in achieving a truly two-dimensional flow in a collapsible channel. Of the many theoretical or numerical studies on a collapsible channel, most have invoked the assumption that the wall can be modelled as a thin membrane instead of solving the governing equations for solid. Consequently, they cannot be used to examine a collapsible channel with tapered wall.

A planar geometry similar to that of the axisymmetric tube is adopted [Figure 1(c)], but with the diameter replaced by the channel height H. On the assumption of symmetry, the computational domain is taken to be the upper half of the channel. Reference quantities and material properties are given in Table 5. As in the axisymmetric tube, flow is induced by decreasing the outlet pressure while inlet pressure is held constant at zero. Wall tension is zero in the undeformed state. Flow rate, plotted as a function of pressure drop in Figure 11, rises to a maximum as downstream pressure is reduced, then, in contrast to the

TABLE 5

Material properties and reference values used in simulations of flow through a two-dimensional collapsible channel

Fluid density, ρ	10^3 kg/m^3
Fluid viscosity, μ	10^{-3} kg/(ms)
Elastic modulus of solid, E	2×10^3 N/m^2
Poisson's ratio of solid, ν	0·3
Reference pressure, $P_{\text{ref}} = E[h_1/(H/2)]^4$	0·2 Pa
Reference flow rate, $Q_{\text{ref}} = H \cdot (P_{\text{ref}}/\rho)^{1/2}$	$1{\cdot}14 \times 10^{-4}$ m^2/s

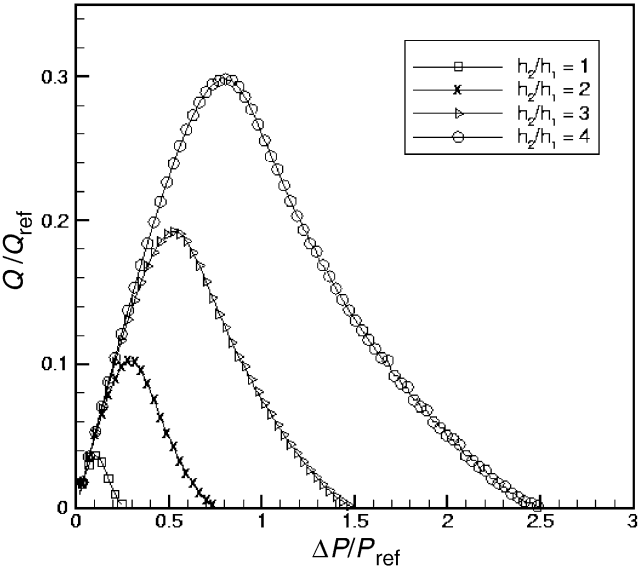

Figure 11. Flow rate in the two-dimensional channel as a function of inlet-to-outlet pressure difference.

axisymmetric tube, falls and approaches zero. This phenomenon was also observed in the recent channel flow studies by Luo & Pedley (2000). Maximal flow rate increases with increasing wall taper, reflecting the increase in average wall thickness and the consequent delay in wall deflection. In each case, the peak in flow rate occurs when the channel is roughly half-way collapsed (Figure 12) with increasing wall taper causing only a slight tendency to move the throat in the upstream direction. At peak flow, the streamlines are smooth, showing little sign of flow separation, both because of the gradual variation in height and because the Reynolds numbers are low (<50 in all cases). Maximum deflection at maximum flow rate is nearly 0·4 H, regardless of the degree of wall taper. Solutions can be continued almost to complete collapse, at which point the flow rates have fallen nearly to zero. The minimum cross-sectional area is a decreasing function of downstream pressure (Figure 13), falling slowly at first, then more rapidly, then seemingly slowly again before the solution is terminated.

Unlike the axisymmetric tube, wave speed in a two-dimensional channel is entirely determined by axial bending stiffness and tension, and approaches zero in the limit of long waves. Therefore, the speed index is ill-defined, as are the concepts of choking or wave-speed flow limitation. Consistent with this, there appears to be no qualitative change in

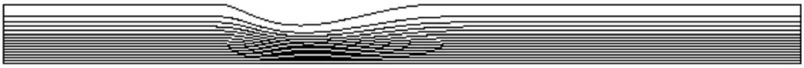

Figure 12. Streamline patterns in the two-dimensional channel at the conditions of maximum flow rate; $h_2/h_1 = 4$ and $\Delta P/P_{ref} = 0{\cdot}85$.

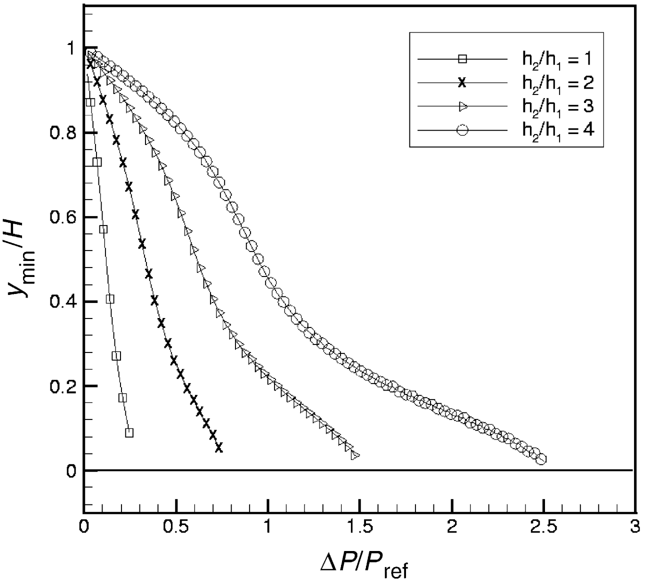

Figure 13. Minimum height of two-dimensional channel as a function of the normalized inlet-to-outlet pressure difference.

flow behavior after the peak in flow rate; height and mean flow speed continue to decrease along the entire length of the channel as downstream pressure is further reduced.

4. SUMMARY

Flow through collapsible tubes has been an active area of research for many years, but was not put on a firm theoretical basis until the development of the one-dimensional theories by Shapiro (1977), Oates (1975), Dawson & Elliot (1977) and Bonis & Ribreau (1978). Since then, the phenomena of flow limitation and flow-induced oscillation have captured the interest of many groups of investigators. Despite considerable advances, however, some of the most fundamental problems remain unanswered. For example, the relationship between flow limitation and flow instability often seen in experiments (Bertram & Raymond 1991) is incompletely understood. And while theoretical models exist that are capable of predicting flow oscillations, there is debate on such fundamental issues as whether or not flow separation is a necessary condition for oscillation.

In this paper, we present two models of steady two-dimensional flow as a step toward the analysis of fully three-dimensional and unsteady conditions. The solutions presented here agree with other published results from experiments and computational analysis, providing some degree of confidence that these same methods, when applied to more general and more realistic conditions, will provide reliable predictions and hence yield some insight into the relevant physical phenomena.

Of more immediate interest, the results presented here shed light on the physics of wave-speed flow limitation. As in free surface waves, flow limitation appears to be governed by the speed of long waves, and is relatively uninfluenced by the fact that shorter waves that propagate at higher speeds must also be present. Unlike one-dimensional theories, however, these results suggest that conditions upstream of the choke point *can* be affected by changes downstream, although the effects are relatively small. The reduction in flow rate, for example, after choking conditions are produced, runs contrary to one-dimensional predictions.

We chose to study tubes with variations in wall thickness in an attempt to avoid the abrupt transitions that are found experimentally when a compliant tube meets a rigid one. Experiments performed in our laboratory (Jaekle 1987; Patel 1993) suggest that many of the same phenomena occur, such as flow limitation and flutter, but do so at a point where conditions are less influenced by the sudden change in wall impedance. We found, not surprisingly, that when the variation in wall thickness is sufficiently steep, with the downstream end stiffer, the point of first collapse moves to the upstream end of the tube or channel. The conditions of this transition would depend on the ratio of the pressure gradient due to flow, and the gradient in wall stiffness. In the axisymmetric tube, the dominant stiffness is due to circumferential compression; in the channel, longitudinal bending. Neither case, however, is likely to be a good predictor of the transition conditions in a real tube, since then the stiffness is largely due to circumferential bending.

We used the full Navier–Stokes equations to describe flow within the collapsible tube and elastic channel, and allowed for a wall with finite thickness that undergoes large deformation. These are all necessary if a realistic simulation is to be created. The true flow field occurring in collapsible tube interacting with an elastic wall has complicated characteristics certain to be influenced by viscous dissipation and possibly flow separation behind the throat of elastic wall. These effects cannot be simulated with inviscid or Stokes flow assumptions. Furthermore, while most previous studies approximate the collapsible tube or channel as a membrane of zero thickness, many of the existing experiments and real occurrences of collapsible tube flow in physiology deal with tubes that are not necessarily thin. Thus, use of the full Navier–Stokes equations and an elastic wall model with finite thickness must ultimately be used to examine realistic situations

The main shortcomings of the present study lie in the assumptions of axisymmetric or two-dimensional geometries, while actual collapsible tube flows are clearly three-dimensional due to buckling combined with rapid axial variations in cross-sectional area. This deficiency can be overcome only by the use of a three-dimensional model. In addition to this, the lack of an accurate turbulence model leads us to neglect turbulence effects even in regions of rapid expansion, potentially leading to somewhat unrealistic predictions within the flow separation region. However, Reynolds numbers considered in the present study are relatively low so the prediction error due to turbulence is likely to be small.

Finally, we note that since these calculations examine only steady state solutions, there is no guarantee that the predicted steady flows are stable. In the few test cases run with the time-dependent equations, no instabilities were observed. However, these tests were far from exhaustive, so we cannot comment more generally on the question of stability, especially in view of the substantial experimental evidence showing that flow-induced oscillations often occur under conditions similar to those studied here. Therefore, the issue of stability remains in question and will need to be considered through more extensive tests using the time-dependent equations.

ACKNOWLEDGEMENTS

We would like to express our gratitude to the National Institutes of Health (HL061794) and the Korea National Computerization Agency for their financial support of this work.

REFERENCES

BATHE, K. J. 1996 *Finite Element Procedures*. Englewood Cliffs, NJ: Prentice-Hall.

BATHE, M. & KAMM, R. D. 1999 A fluid–structure interaction finite element analysis of pulsatile blood flow through a compliant stenotic artery. *ASME Journal of Biomechanical Engineering* **121,** 361–369.

BATHE, K. J., ZHANG, H. & WANG, M. H. 1995 Finite element analysis of incompressible and compressible fluid flows with free surfaces and structural interactions. *Computers and Structures* **56,** 193–213.

BATHE, K. J., ZHANG, H. & ZHANG, X. 1997 Some advances in the analysis of fluid flows. *Computers and Structures* **64,** 909–930.

BERTRAM, C. D. 1986 Unstable equilibrium behavior in collapsible tubes. *Journal of Biomechanics* **19,** 61–69.

BERTRAM, C. D. & PEDLEY, T. J. 1982 A mathematical model of unsteady collapsible tube behavior. *Journal of Biomechanics* **15,** 39–50.

BERTRAM, C. D. & RAYMOND, C. J. 1991 Measurements of wave speed and compliance in a collapsible tube during self-excited oscillations: a test of the choking hypothesis. *Medical and Biological Engineering and Computing* **28,** 493–500.

BONIS, M. & RIBREAU, C. 1978 Etude de quelques propriétés de l'écoulement dans une conduite collabable. *La Houille Blanche* No. 3/4, 165–173.

BROWER, R. W. & SCHOLTEN, C. 1975 Experimental evidence on the mechanism for the instability of flow in collapsible vessels. *Medical and Biological Engineering* **13,** 839–845.

CARO, C. G., PEDLEY, T. J., SCHROTER, R. C. & SEED, W. A. 1978 *The Mechanics of the Circulation*. Oxford: Oxford University Press.

CONRAD, W. A. 1969 Pressure-flow relationships in collapsible tubes. *IEEE Transactions Biomedical Engineering* **BME 16,** 284–295.

DAWSON, S. V. & ELLIOT, E. A. 1977 Wave-speed limitation on expiratory flow—a unifying concept. *Journal of Applied Physiology* **43,** 498–515.

HAGGBLAD, B. & SUNDBERG, J. A. 1983 Large strain solutions of rubber components. *Computers and Structures* **17,** 835–843.

HEIL, M. & PEDLEY, T. J. 1995 Large axisymmetric deformation of a cylindrical shell conveying a viscous flow. *Journal of Fluids and Structures* **9,** 237–256.

HEIL, M. 1997 Stokes flow in a collapsible tubes: computation and experiment. *Journal of Fluid Mechanics* **353,** 285–312.

JAEKLE, D. E. 1987 Critical transitions associated with steady flow in collapsible tubes with varying wall stiffness. M.S. Thesis, MIT.

KAMM, R. D. & PEDLEY, T. J. 1989 Flow in collapsible tubes: a brief review. *ASME Journal of Biomechanical Engineering* **111,** 177–179.

KECECIOGLU, I., MCCLURKEN, M. E., KAMM, R. D. & SHAPIRO, A. H. 1981 Steady, supercritical flow in collapsible tubes. Part 1. Experimental observations. *Journal of Fluid Mechanics* **109,** 367–389.

LUO, X. Y. & PEDLEY, T. J. 1995 A numerical simulation of steady flow in a 2-D collapsible channel. *Journal of Fluids and Structures* **9,** 149–174.

LUO, X. Y. & PEDLEY, T. J. 1996 A numerical simulation of unsteady flow in a 2-D collapsible channel. *Journal of Fluid Mechanics* **314,** 191–225.

LUO, X. Y. & PEDLEY, T. J. 2000 Multiple solutions and flow limitation in collapsible channel flows. *Journal of Fluid Mechanics* **420,** 301–324.

MCCLURKEN, M. E., KECECIOGLU, I., KAMM, R. D. & SHAPIRO, A. H. 1981 Steady supercritical flow in collapsible tubes: Part 2. Theoretical studies. *Journal of Fluid Mechanics* **114,** 60–67.

OATES, G. C. 1975 Fluid flow in soft-walled tubes: I. Steady flow. *Medical and Biological Engineering* **13,** 773–778.

Patel, N. K. 1993 A study of flow limitation and flow-induced oscillations during airflow through collapsible tubing. B.S. Thesis, MIT.

Pedley, T. J. 1992 Longitudinal tension variation in a collapsible channel: a new mechanism for the breakdown of steady flow. *ASME Journal of Biomechanical Engineering* **99,** 126–147.

Rast, M. P. 1994 Simulataneous solution of the Navier–Stokes and elastic membrane equations by a finite-element method. *International Journal of Numerical Methods in Fluids* **19,** 1115–1135.

Shapiro, A. H. 1977 Steady flow in collapsible tubes. *ASME Journal of Biomechanical Engineering* **99,** 126–147.

Stergiopulos, N., Moore, J. E., Strassle, A., Ku, D. N. & Meister, J. J. 1993 Steady flow tests and demonstration of collapse on models of compliant axisymmetric stenosis. *Advances in Bioengineering*, **BED-26,** 455–458.

Zmindak, M. & Grajciar, I. 1997 Simulation of the aquaplane problem. *Computers and Structures* **64,** 1155–1164.